Salvatore Greco, Carlo; Paolillo, Gerardo; Ianiro, Andrea; Cardone, Gennaro; de Luca, Luigi (2018). Effects of the stroke length and nozzle-to-plate distance on synthetic jet impingement heat transfer, *International Journal of Heat and Mass Transfer*, v. 117, pp.: 1019-1031.

DOI: https://doi.org/10.1016/j.ijheatmasstransfer.2017.09.118

Effects of the stroke length and nozzle-to-plate distance on synthetic jet impingement heat transfer

Carlo Salvatore Greco[a,*], Gerardo Paolillo[a], Andrea Ianiro[b], Gennaro Cardone[a], Luigi de Luca[a]

[a] *Dipartimento di Ingegneria Industriale Sezione Aerospaziale, Universitá di Napoli Federico II, 80125 Piazzale Tecchio 80, Napoli, Italy*
[b] *Aerospace Engineering Group, Universidad Carlos III de Madrid, 28911 Av. de la Universidad 30, Laganés, Spain*

Abstract

This study focuses on the combined effect of the nozzle-to-plate distance and of the stroke length on the cooling performances of impinging synthetic jets. Infrared thermography is used as temperature transducer in conjunction with the heated thin foil heat transfer sensor to measure time- and phase-averaged convective heat transfer. All the experiments have been performed at a fixed Reynolds number equal to 5,250, while different values of the dimensionless stroke length (L_0/D equal to 5, 10 and 20) and nozzle-to-plate distance (H/D between 2 and 10) have been considered. At high L_0/D, the heat transfer behaviour resembles that of a continuous impinging jet. It is characterized by a time-averaged stagnation Nusselt number maximum between H/D equal to 4 and 6 and inner and outer ring-shaped regions of Nusselt number maximum at short H/D. These two regions are replaced by a bell-shaped distribution at higher nozzle-to-plate distances. The existence of these regions are clearly observed through the phase-averaged heat transfer measurements. At short H/D, the heat transfer evolution reveals the simultaneous presence of two outer ring-shaped regions. The external outer region is ascribed to the strong coherence of the primary vortex ring, while the internal one is mainly due to the vortex rings generated by the Kelvin-Helmholtz instability along the trailing jet shear

*Corresponding author
Email address: carlosalvatore.greco@unina.it (Carlo Salvatore Greco)

layer. At high H/D, the internal outer-ring shaped region disappears because of the weakening of the trailing jet Kelvin-Helmholtz vortex rings. In opposition, at short L_0/D, the time-averaged stagnation point Nusselt number is found to have a maximum at lower values of H/D, and no inner ring-shaped region of heat transfer maximum is observed. This region is not present, at low dimensionless stroke lengths, because of the weakness and reduced extent of the trailing jet in the flow field. Indeed, the phase-averaged measurements mainly show the heat transfer caused by the impinging primary vortex ring. Despite the weakness of the trailing jet, the outer ring-shaped region of heat transfer maximum is observed at short H/D because of the presence of a strong primary vortex ring. In addition to that, the dimensionless stroke length and nozzle-to-plate distance also affect the heat transfer fluctuations, which decrease as L_0/D decreases and/or H/D increases.

Keywords: IR Thermography; synthetic jets; heat transfer; vortex ring; trailing jet.

---

1. Introduction

Impinging jets are widely recognized and quoted in the scientific literature [1, 2, 3] as one of the most effective techniques to achieve high convective heat transfer rates, thus they are one of the preferred choices for high performance heating/cooling applications. Recent literature is focusing on the design and optimization of advanced impinging jet devices in order to apply them in specific fields such as the electronic cooling. In particular, several literature works [4, 5, 6, 7] deal with the exploitation of impinging synthetic jets. Synthetic jets are jets with zero-net-mass-flux, directly "synthesized" from the fluid system in which the jet actuator is embedded. Such a feature obviates the need for an external input piping, making them ideal for low cost and reduced space applications.

A synthetic jet is generated by a membrane oscillating in a cavity, which produces a periodic volume change and therefore a periodic pressure variation.

As the membrane oscillates, the fluid is periodically entrained into and expelled out of the cavity through an orifice. Such a behaviour is usually modelled by using a lumped element method [8, 9, 10, 11]. During the suction portion of the cycle, the flow field could be considered as one induced by a sink, which coincides with the orifice. On the contrary, during the ejection portion of the cycle, a vortex ring is formed near the orifice. Under certain operating conditions [12], this vortex ring convects away from the orifice to form a time-averaged jet near the jet axis [13]. The velocity temporal variation at the orifice is used to define the parameters of the problem. In particular, the stroke length L_0 is defined as the integral of the axial velocity at the nozzle exit over the ejection part of the cycle, which correspond to half of the total actuation period τ:

$$L_0 = \int_0^{\tau/2} u_a(t)dt \tag{1}$$

where u_a is the exit velocity on the jet axis; accordingly, the reference velocity can be defined as:

$$U_0 = \frac{L_0}{\tau} \tag{2}$$

from which it is evident that U_0 is a characteristic velocity over the whole cycle of period τ. Following Smith and Glezer [13], the flow field of synthetic jets is characterized by a proper Reynolds number and a dimensionless stroke length, which is equal to the inverse of the Strouhal number [14] defined as:

$$Re = \frac{\rho U_0 D}{\mu} \tag{3}$$

$$\frac{1}{Sr} = \frac{L_0}{D} \tag{4}$$

where ρ is the air density, μ is the air dynamic viscosity and D is the nozzle

diameter.

Research efforts on synthetic jets for cooling applications are quite recent and are limited mostly to the last decade, apart from the pioneering work of Gutmark et al. [15]. One of the first works is due to Mahalingam and Glezer [16], who studied the synthetic jet impingement for the enhancement of the thermal performances of heat sinks. The use of synthetic jets enabled to reduce the temperature of the cooled surface from 71.5 to 36℃ and to provide, at the same time, a power dissipation of 20-40% higher than that of the same heat sink coupled with a fan with similar power input. The promising performances of synthetic jets were later confirmed by the studies of Chaudhari et al. [4]. They showed that the Nusselt number of a synthetic jet, at a Reynolds number up to 4,000, is comparable to that of a circular jet impinging on a plane surface. Furthermore, they argued that the performances of synthetic jets could overcome those of circular jets at higher Reynolds number [4].

Several researches focused on the quantitative characterization of the heat transfer performances in several operating conditions [5, 17, 18, 19]. In particular, heat transfer correlations for impinging synthetic jets are reported by Arik and Icoz [20] and Persoons et al. [21]. Arik and Icoz [20] established a closed form correlation to predict the heat transfer coefficient as a function of the Reynolds number, the axial distance, the orifice size and the jet driving frequency. They observed that the cooling performances of synthetic jets peak at their resonance frequencies, and that the effect of the axial distance on the heat transfer becomes more important as the jet driving frequency increases. Persoons et al. [21] proposed a general correlation for the stagnation point Nusselt number including the effect of all appropriate scaling parameters: the Reynolds number ($500 \leq Re \leq 1{,}500$), the jet-to-surface spacing ($2 \leq H/D \leq 16$) and the dimensionless stroke length ($2 \leq L_0/D \leq 40$).

The great variety of parameters, involved in the problem, makes this analysis quite complex. While in continuous jets, the heat transfer coefficient depends on the nozzle-to-plate distance, the radial position on the plate, the turbulence

intensity and the Reynolds number, in synthetic jets one can argue that the dimensionless stroke length (or, equivalently, the Strouhal number) plays a key role.

As a matter of fact, the dimensionless stroke length influences the flow morphology of synthetic jets, as experimentally studied by McGuinn et al. [22] through high speed PIV and hot wire anemometry techniques. McGuinn et al. [22] stated that, increasing the stroke length up to $L_0/D = 4$, a free synthetic jet reveals an increasing vortex strength. In particular, the increase of the vortex strength ceases at $L_0/D = 8$ but, for these larger stroke lengths (i.e. $4 \leq L_0/D < 8$), an additional quantity of fluid, called trailing jet, is ejected after the formation of the vortex ring, following and widening the vortex ring itself. At $8 \leq L_0/D < 16$, this trailing jet destabilizes the vortex ring promoting mixing, and, for higher L_0/D, it represents the most relevant flow feature, because it overtakes the vortex ring resulting in a highly turbulent intermittent jet flow.

Consistently, the dimensionless stroke length also affects the flow field organization of an impinging synthetic jet, as investigated by Greco et al. [23]. Greco et al. [23] analysed the behaviour of a turbulent impinging synthetic jet for three dimensionless stroke lengths and three orifice-to-plate distances. They revealed that, at low dimensionless stroke lengths, the main presence of the vortex ring in the flow field causes a greater jet width and a lower centreline velocity. Differently, at high dimensionless stroke lengths, they found that the presence of the trailing jet completely affects the flow field morphology resulting in an opposite behaviour: greater centreline velocity and lower jet width. Greco et al. [23] also noticed that the phase correlated kinetic energy increases with the dimensionless stroke length, because of a greater amplitude of the external oscillation introduced in the flow field through the orifice exit. In opposition, the turbulent kinetic energy decreases at high dimensionless stroke lengths, because of the strong presence of the trailing jet and its inherent potential core. According to their results [23], at high dimensionless stroke lengths, the impinging synthetic jet behaviour resembles more that of a continuous jet with its own characteristics, while, at low dimensionless stroke lengths, such a behaviour is

very close to that of a train of impinging vortex rings.

In particular, the schematic topology of the instantaneous flow field of a synthetic jet, during its impinging phase, is shown in Figure 1. At high dimensionless stroke lengths (Figure 1, left), the synthetic jet flow field consists of two main structures: the trailing jet and the primary vortex ring. The trailing jet is the part of the flow field that follows the primary vortex ring. This part of the impinging flow field is characterized by a region of low turbulence, called potential core, surrounded by a shear layer zone. Along this shear layer region, the Kelvin-Helmholtz instability causes the generation of multiple vortex rings [23]. Such vortex rings arrive at the impingement plate after the primary vortex ring, which is generated at the beginning of the synthetic jet expulsion stroke. This primary vortex ring and all the successive Kelvin-Helmholtz vortex rings cause the generation of secondary counter-rotating vortex rings near the impingement plate, during their sweeping phase.

At low dimensionless stroke lengths (Figure 1, right), the flow field has a completely different morphology. No trailing jet is present, and the flow field is characterized by the simultaneous presence of multiple primary vortex rings, which impinge on the plate, separately. The distance between such vortex rings decrease with the decreasing of L_0/D [24]. During the sweeping phase, each primary vortex ring gives rise to a secondary counter-rotating vortex ring near the impingement plate. Differently from the previous case, at low dimensionless stroke lengths, the secondary vortex rings are generated only by the passage of the primary vortex rings on the impingement plate.

These two structures (i.e., vortex ring and trailing jet) completely characterize the flow field morphology of an impinging synthetic jet, and, consequently, its heat transfer process. The influence of such structures on the flow field is tuned by the dimensionless stroke length (L_0/D). This parameter determines the presence [22] and extension [23] of the trailing jet and the dynamics of the vortex ring [23], which are the main heat transfer mechanisms as shown by Valiorgue et al. [5], Greco et al. [7] and Silva-Lanca and Ortega [25].

The recent knowledge on fluid mechanics of impinging synthetic jets, which

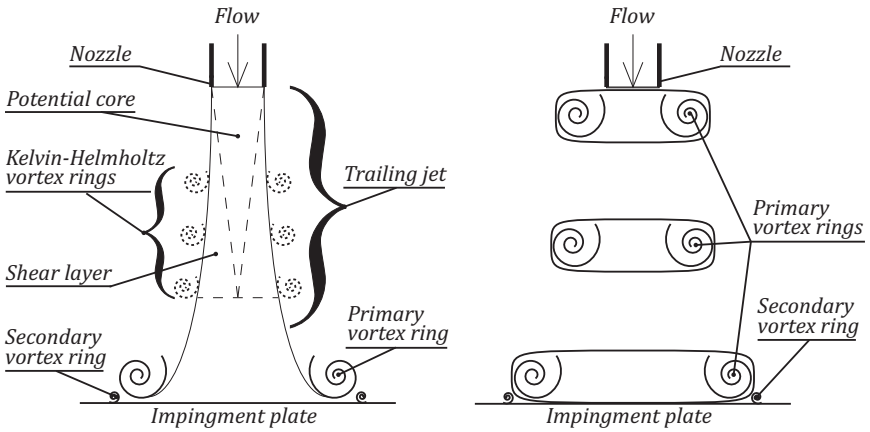

Figure 1: Schematic morphology of the instantaneous flow field of a turbulent impinging synthetic jet, characterized by high (left) and low (right) dimensionless stroke lengths.

has shed light on the influence of the dimensionless stroke length on the flow field organization, motivates our study on the implications of various dimensionless stroke lengths on the synthetic jet heat transfer performances. From the above discussion, it is clear that synthetic jets are characterized by one more degree of freedom with respect to continuous jets, since the dimensionless stroke length is a relevant parameter.

In order to deeply understand the effect of the dimensionless stroke length on the complete heat transfer mechanisms of turbulent impinging synthetic jets, time-resolved heat transfer measurements are necessary. Indeed, to the authors' knowledge, very few studies deal with the heat transfer of turbulent impinging synthetic jets [4, 7, 17, 26], differently from those on laminar impinging synthetic jets [5, 16, 27, 28, 29, 30, 31, 32], and only some of them report the spatial heat transfer distributions and their temporal evolution [7, 17].

The aim of this work is to investigate the influence of the dimensionless stroke length and dimensionless nozzle-to-plate distance on the heat transfer behaviour of a turbulent impinging synthetic jet. The heat transfer distribution and its temporal evolution are analysed, considering the physics of the impinging synthetic jet flow field [23, 33] that causes such a thermal footprint. In the

present study, the heat transfer coefficients of the impinging synthetic jet are measured at a Reynolds number of 5,250 and for three different values of the dimensionless stroke length, namely 5, 10 and 20. For each value of the stroke length, several values of the nozzle-to-plate distance are chosen (in the range 2 $\leq H/D \leq 10$). The convective heat transfer coefficient is measured with the heated thin foil heat transfer sensor [34, 35], and an infrared (IR) camera is used as temperature transducer. Time- and phase-averaged data are reduced and presented in non-dimensional form as Nusselt number.

2. Experimental setup and data reduction

The experimental apparatus is sketched in Figure 2. It includes a constantan foil, which is 200 mm wide, 450 mm long and 50 μm thick, constituting the impingement plate. The foil is steadily and uniformly heated by Joule effect, and it is cooled by the synthetic air jet impinging on it. The Joule heating is obtained by applying a steady voltage difference to the edges of the foil, by using a stabilized DC power supply and two couples of bus bars, made of copper, clamped at the shortest sides of the foil. The very large equivalent cross section (weighted with the electrical resistivity) of the bus bars, with respect to that of the heated foil, ensures negligible voltage drop through them. The electrical contact between the bus bars and the foil is enhanced by putting there an indium wire (about 1 mm in diameter). The impingement plate is positioned horizontally with the synthetic jets impinging vertically from below. The circular synthetic air jet is generated by means of the device shown in Figure 2, that substantially coincides with the device used and already well characterized by the authors [7, 33, 36, 37].

A loudspeaker, having a diameter of 270 mm, confines a cavity with a volume V equal to 2×10^{-3} m^3. The jet is issued from a pipe, attached to the cavity, which has a length L of 200 mm and an inner diameter D of 22 mm. Experiments are performed for three values of the dimensionless stroke length L_0/D, namely 5, 10 and 20. The dimensionless nozzle-to-plate distance H/D is

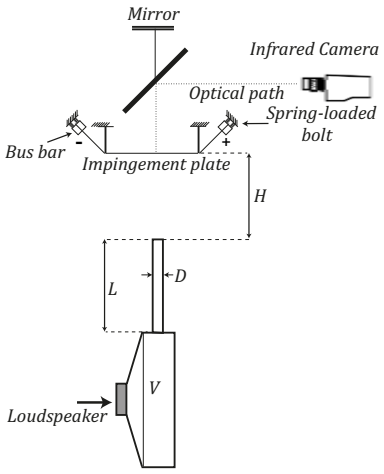

Figure 2: Sketch of the experimental apparatus.

varied between 2 and 10. All the experiments are performed at the same value of the Reynolds number (5,250). The Reynolds number (Eq.3) and the Strouhal number (Eq.4) are evaluated using the characteristic velocity U_0 (Eq.2). Such a velocity is calculated by means of phase-averaged Particle Image Velocimetry (PIV) measurements, as previously done in Greco et al. [36]. During these PIV measurements, the pressure oscillation inside the cavity has been measured by using an Honeywell HSCDRRN002NDAA5 pressure transducer, and then this pressure value has been monitored during all the tests. The loudspeaker, used in the present experiments (CIARE HS250), has a free-space resonance frequency of 25 Hz, a nominal diameter of 208 mm and an equivalent oscillating mass of 56 g. It is supplied with a sinusoidal input signal with a frequency f equal to 8, 16 and 32 Hz, for the cases L_0/D equal to 20, 10 and 5, respectively. The frequency and the input signal amplitude are varied in order to obtain synthetic jets characterized by the same Reynolds number and with different values of the stroke length. The input signal is generated by a signal generator DILIGENT Analog Discovery™ and it is amplified by a Hi- Fi amplifier (Kenwood KAC-6405).

An IR camera (CEPID JADE III, 320 x 240 focal plane array) measures

the foil surface temperature with a spatial resolution of 0.94 pixels/mm (20.68 pixels/D). The focal plane array is cropped (160 x 120 pixels) in order to increase the sampling frequency (up to 480 Hz). In order to reconstruct the temporal, phase-averaged, variation of the convective heat transfer on the impingement plate, 30 phases of the cycle are sampled. The sampling frequency f_s is set to 240 and 480 Hz for the cases $f = 8$ Hz and $f = 16$ Hz, respectively, in order to acquire 200 images per phase (for a total of 6000 images). In the case $f = 32$ Hz, the same number of images per phase is obtained by carrying out two successive acquisitions at a sampling rate $f_s = 480$ Hz with a relative time delay equal to $0.5 f_s$. The IR camera is accurately calibrated with a blackbody for the whole measurement range; the noise equivalent temperature level of the camera is about 25 mK, and the rms error from the blackbody calibration is less than 0.1 K. The foil rear surface is coated with high emissivity enamel (with hemispherical emissivity $\epsilon = 0.95$) in order to increase the accuracy of temperature measurements.

The IR camera is used in conjunction with the heated thin foil heat transfer sensor [34, 35]. The present experimental methodology has been assessed along several years, and it is documented in previous works on circular impinging jets [38, 39, 40, 41, 42, 43] and synthetic jets [7]. Applying the local unsteady energy balance to the foil, the convective heat transfer coefficient h can be evaluated as:

$$h(x,y,t) = \frac{\dot{q}_j - \dot{q}_r - \dot{q}_k - \dot{q}_n - \rho_{foil} c \delta \dfrac{dT_w}{dt}}{T_w - T_{aw}} \tag{5}$$

where $\dot{q}_j$ is the Joule heat flux, $\dot{q}_r$ the radiation heat flux, $\dot{q}_n$ the natural convection heat flux on the rear foil surface, $\dot{q}_k$ the tangential conduction heat flux, ρ_{foil} the constantan density, c the constantan specific heat, δ the foil thickness, dT_w/dt the time derivative of the wall temperature T_w and T_{aw} the adiabatic wall temperature. T_w and T_{aw} are the temperature of the foil in non-adiabatic and adiabatic conditions, respectively.

The phase-averaged convective heat transfer coefficients are determined from Eq.5 by replacing the instantaneous quantities with the corresponding phase-averaged ones. Differently, the time-averaged convective heat transfer coefficients are obtained as:

$$\overline{h}(x,y) = \frac{\dot{q}_j - \overline{\dot{q}_r} - \overline{\dot{q}_k} - \overline{\dot{q}_n}}{\overline{T_w} - \overline{T_{aw}}} \tag{6}$$

where the upper bar indicates the time-averaged quantities (evaluated for present experiments as the temporal average of all the 6000 acquired IR images).

The temperature distribution is measured observing, with the IR camera, the bottom face of the impinged plate, opposite to the jet impingement, through a mirror (see Figure 2). The temperature is considered constant through the foil thickness, because the Biot number ($Bi = \overline{h}s/\lambda_f$ where λ_f is the foil thermal conductivity) and the inverse of modified Fourier number ($Fo_f = \alpha/\pi f \delta^2$ where α is the foil thermal diffusivity) are small with respect to unity[44]. Each experiment consists of two acquisitions: "hot acquisition" with electric current on and "cold acquisition" with electric current off. The first acquisition allows measuring T_w, while the second one provides T_{aw} [38, 40]. The net radiation heat flux to the ambient is estimated as:

$$\dot{q}_r = \epsilon\sigma(T_w^4 - T_{amb}^4) \tag{7}$$

where σ is the Stefan Boltzmann constant and T_{amb} is the ambient temperature ($\dot{q}_r$ is found to be at worst 16% of $\dot{q}_j$ at distances from the center of impingement lower than three diameters). The thermal losses for tangential conduction (that are found being at worst equal to 2%) are estimated as [40, 45]:

$$\dot{q}_k = -\lambda_f \delta \nabla^2 T_w \tag{8}$$

where $\nabla^2 T_w$ is the in-plane Laplacian of the temperature.

Losses due to natural convection are mostly related to those of a heated plate facing upward [46], whose empirical correlation is reported in [47]. Applying this correlation, the natural convection losses are estimated to be, at worst, equal to 16.8% of $\dot{q_j}$ with an accuracy of 10% of the total value of said losses.

The procedure to calculate the unsteady term dT_w/dt consists of filtering the temperature signals through a POD based filter [37] coupled with a spatio-temporal polynomial filter, and then phase-averaging. As a matter of fact, the temperature signal is affected by the measurement noise, which is alleviated through this POD-based filter. Such a filter is then coupled with a spatio-temporal second order polynomial filter, employing a stencil of 11×11 pixels in space and 5 snapshots in time, in order to reduce also residual spatial incoherence. Finally, in order to improve the accuracy of the derivatives, a phase averaging process is performed over the 200 samples acquired for each phase.

The measured values of the convective heat transfer coefficient are reported in non-dimensional form: time-averaged Nusselt number $\overline{Nu} = \overline{h}D/k$ (k is the thermal conductivity of air at the film temperature defined as $(T_w + T_{aw})/2$), phase-averaged Nusselt number $Nu_\varphi = h_\varphi D/k$ and standard deviation of phase-averaged Nusselt number fields Nu'.

The typical values and uncertainties for the time- and phase-averaged measurements are summarized in Table 1. Considering such uncertainties and the error analysis of Moffat [48], the estimated error for Re (considering Eqs.2 and 3) is less than 1.5%, for Sr is less than 1% (considering Eq.4), for Nu (considering Eq.5) is less than 4%, for Nu_φ (considering Eq.6) is less than 8% and for Nu' is less than 5%. All these uncertainties are based on a 95% confidence level.

3. Results and Discussion

In the following, the time-averaged and phase-averaged results are reported and discussed. Since the investigated phenomenon is axisymmetric, all the Nusselt number time-averaged profiles have been averaged azimuthally in order

Table 1: Control parameters and their uncertainty.

Parameter	*Typical value*	*Typical error*
T_{aw}	305 K	0.35 K
T_w	320 K	0.35 K
$T_w - T_{aw}$	14–15 K	0.2 K
T_{amb}	304 K	0.05 K
v	1.32 V	0.01 V
i	57.5 A	0.42 A
ϵ	0.95	0.01
ρ_{foil}	8920 kg/m^3	8.92 kg/m^3
c	393 J/kgK	8 J/kgK
s	50 x 10^{-6} m	1 x 10^{-6} m
dT_w/dt	$\pm$0.928 K/s	0.0645 K/s
ρ	1.225 kg/m^3	1.225 x 10^{-2} kg/m^3
U_0	3.6 m/s	0.02 m/s
D	0.022 m	0.1 x 10^{-3} m
μ	1.8 x 10^{-5} Pa s	1.8 x 10^{-7} Pa s

to reduce the noise. In the phase-averaged results section, the reference phase $\varphi = 0°$ is chosen as the phase in which the Nusselt number time derivative in the stagnation point switches from negative to positive. For the sake of clarity, ten phases with a phase step of $\Delta\varphi = 36°$, for six operating conditions (i.e., H/D equal to 2 and 10 for all the L_0/D values), are discussed in the phase-averaged results section.

3.1. Time-averaged results

Figure 3 reports the variation of the stagnation point Nusselt number as a function of H/D. At $L_0/D = 20$, $\overline{Nu}_0$ increases with increasing nozzle-to-plate distance, reaching its maximum value between H/D equal to 4 and 6, before decreasing. Such a behaviour can be explained by the existence of

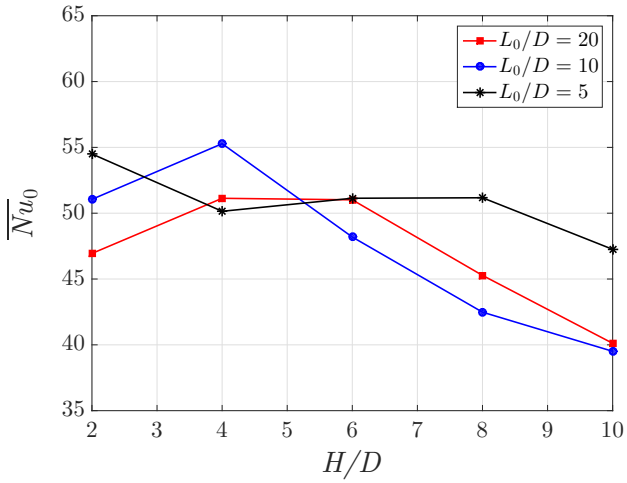

Figure 3: Stagnation Nusselt number for each value of L_0/D (i.e., 5, 10 and 20) and H/D (i.e., 2, 4, 6, 8 and 10) at Reynolds number equal to 5,250.

a potential-core-like region in the synthetic jet flow field, as shown by Greco et al. [36]. Indeed, the presence of a trailing jet, in the synthetic jets with high dimensionless stroke lengths, causes the existence of a triangular region of low turbulence intensity nearby the centreline axis, as occurs for continuous jets [49]. The axial extent of this region determines the nozzle-to-plate distance at which the maximum stagnation point heat transfer can be achieved [2]. In fact, at the end of this region, the turbulence intensity raises, while, simultaneously, the axial velocity diminishes [36]. As the turbulence increase does no longer overwhelm or compensate the velocity decrease, the stagnation Nusselt number value decreases [2], as occurs for $H/D > 6$.

In agreement with Greco et al. [23], the potential core length of synthetic jets decreases with decreasing stroke length and, for this reason, the maximum stagnation Nusselt number at $L_0/D = 10$ is attained at a shorter nozzle-to-plate distance (i.e., $H/D = 4$). As a matter of fact, at $L_0/D = 10$, $\overline{Nu_0}$ increases with H until $4D$ and then it drops. At $H/D \leq 4$, $\overline{Nu_0}$ attains values higher than those observed for $L_0/D = 20$, while this behavior switches for $H/D \geq 6$, except $H/D = 10$ where the two $\overline{Nu_0}$ values are almost equal. This result

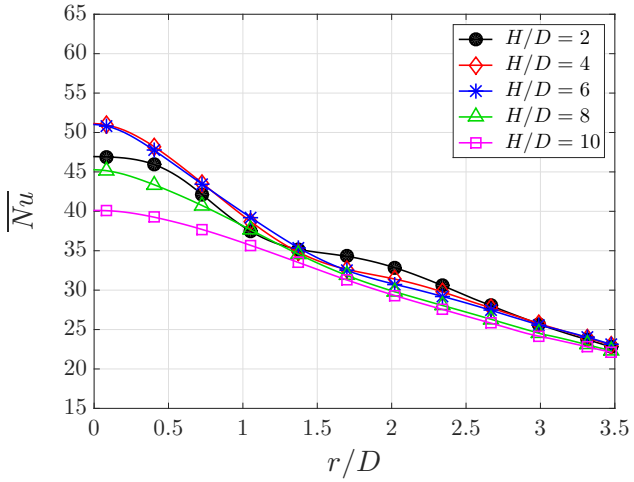

Figure 4: Stagnation Nusselt number for $L_0/D = 20$ and each H/D (i.e., 2, 4, 6, 8 and 10) at Reynolds number equal to 5,250.

could be ascribed to the fact that in such conditions the values of the impinging axial velocity and of the turbulent kinetic energy are greater for $L_0/D = 10$ at $H/D \leq 4$, while larger for $L_0/D = 20$ at $H/D = 6$ [23].

At the lowest investigated stroke length (i.e., $L_0/D = 5$), the synthetic jet flow field is mainly characterized by a train of convecting vortex rings, according to McGuinn et al. [22]. The absence of a strong trailing jet causes the absence of a prominent stagnation Nusselt number peak for all the investigated nozzle-to-plate-distances. Indeed, $\overline{Nu_0}$ shows a local maximum at $H/D = 2$, then a plateau for $4 \leq H/D \leq 8$ before slightly decreasing. Such a behaviour is in agreement with that of the centerline streamwise time-averaged velocity of synthetic jets characterized by low L_0/D values [50].

In Figure 4, the radial $\overline{Nu}$ profiles for $L_0/D = 20$ and each nozzle-to-plate distance are shown. At the shortest nozzle-to-plate distance, the time-averaged Nusselt number distribution shows a plateau around the stagnation point ($r/D \leq 0.3$). Such a plateau corresponds to the region where the jet potential core impinges, over which the axial velocity profile remains substantially constant [23, 33]. Outside of the plateau region, $\overline{Nu}$ decreases with the radial

distance, but, further downstream, the rate of decrease is slowed down until reaching a minimum value at $r/D = 1.55$, where a second inflection point in the $\overline{Nu}$ profile is observed. While the inner inflection point ($r/D = 0.75$) is related to the deceleration of the wall jet when moving away from the stagnation region, the outer one is essentially related to the formation of secondary vortex rings attached to the plate [7, 23, 33]. The secondary vortex rings originate from the unsteady separation induced by the adverse pressure gradient associated with the passage of the primary vortex ring and the vortex rings generated by the Kelvin-Helmholtz instability along the shear layer of the trailing jet. Since, during their propagation along the wall, the secondary vortex rings move away from it [51], their effect upon the time-averaged heat transfer is principally observed around the region of formation, resulting in the outer inflection point. This inflection point is still observed at $H/D = 4$ (at $r/D = 1.9$) and barely visible at $H/D = 6$. At higher nozzle-to-plate distances, the $\overline{Nu}$ profile exhibits only one inflection point associated with the radial deceleration of the wall jet outside of the stagnation region. The absence of the outer inflection point is due to the weakening of the primary vortex ring [33] and of the trailing-jet Kelvin-Helmholtz vortex rings [3], which are no longer able to initiate strong secondary vortex rings. For $H/D \geq 8$, the $\overline{Nu}$ profile is definitely bell-shaped.

A similar behavior is shown at $L_0/D = 10$ (Figure 5). At $H/D = 2$, the plateau region near the stagnation region is present but it is less wide than that observed at $L_0/D = 20$, due to the limited extent of the potential-core-like region. Furthermore, the outer inflection point can be observed at similar radial positions for both the shortest dimensionless nozzle-to-plate distances (i.e., r/D equal to 1.6 and 1.9 for H/D equal to 2 and 4, respectively). Such inflection points are less definite because there is no contribution of the Kelvin-Helmholtz vortex rings due to the limited extent of the trailing jet (see phase-averaged measurements at $H/D = 2$ for $L_0/D = 10$). At H/D equal to 6 and 8, the $\overline{Nu}$ profile near the stagnation region ($r/D \leq 1.5$) shows a less steep decrease than those at $L_0/D = 20$, while, at $H/D = 10$, the $\overline{Nu}$ profiles are similar.

The $\overline{Nu}$ profiles, for $L_0/D = 5$, are reported in the Figure 6. At the shortest

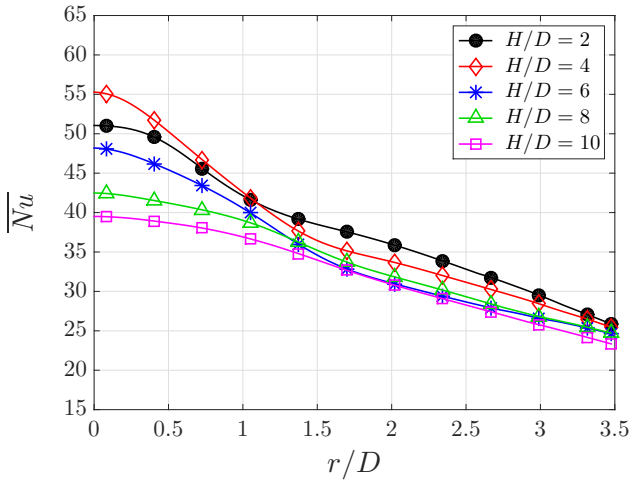

Figure 5: Stagnation Nusselt number for $L_0/D = 10$ and each H/D (i.e., 2, 4, 6, 8 and 10) at Reynolds number equal to 5,250.

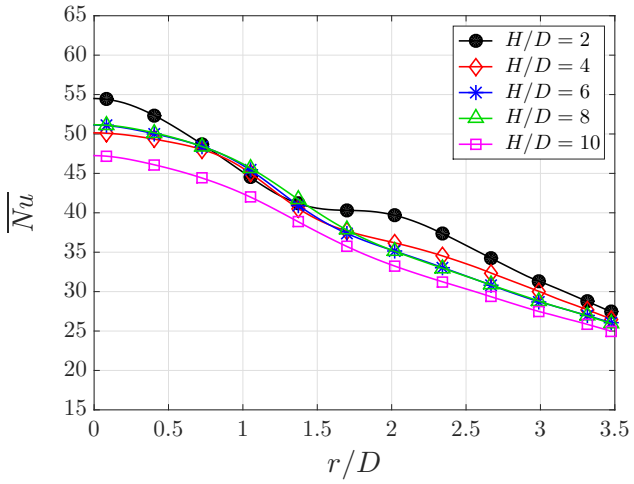

Figure 6: Stagnation Nusselt number for $L_0/D = 5$ and each H/D (i.e., 2, 4, 6, 8 and 10) at Reynolds number equal to 5,250.

considered H/D, the maximum $\overline{Nu}$ value is attained in the stagnation point, but no plateau is observed near the stagnation region because of the absence of the potential core region. The outer inflection point is detected at $r/D = 1.7$, slightly farther from the stagnation point than the previous L_0/D values. This inflection point is clearly visible, more than those at higher L_0/D, because it is only due to the intense secondary vortex rings generated by the passage of only strong primary vortex rings. Indeed, at this low L_0/D, no contribution of Kelvin-Helmholtz vortex rings is present (in contrast with the case at $L_0/D = 20$) since they are not generated due to the weakness and very short extent of the trailing jet. Furthermore, the absence of a long trailing jet does not cause the presence of a wall jet (see phase-averaged measurements at $H/D = 2$ for $L_0/D = 20$ and 10), which mitigates, on the average, the strength of the heat transfer peak caused by the secondary vortex rings generation. As H/D increases, the $\overline{Nu}$ profile starts being characterized by a flatter distribution near the stagnation region ($r/D \leq 1$ for $4 \leq H/D \leq 8$). Moreover, as for the cases at higher L_0/D, the outer inflection point is still observed at $r/D = 2$ for $H/D = 4$, while it disappears for $H/D \geq 6$, where the $\overline{Nu}$ profiles assume a bell-shaped distribution.

In Figure 7, the radial Nu' distributions for $L_0/D = 20$ and each nozzle-to-plate distances are represented. At $H/D = 2$, the Nu' profile is characterized by two local minima, at r/D equal to 0 and 1.2, and two local maxima, at r/D equal to 0.4 and 1.6, and a monotonic decrease for $r/D \geq$1.6. The two Nu' maxima are located in those regions commonly called in literature [3] inner and outer ring-shaped regions of maximum heat transfer (as shown later in the phase-averaged results section). At $H/D = 4$, the shape of the Nu' profile is different: the first local minimum and maximum are replaced by a unique maximum at $r/D = 0$, while the second local maximum is replaced by an inflection point located at $r/D = 1.7$. The limited potential core extent is the cause underlying the absence of the inner ring-shaped region of maximum heat transfer, as also reported by Greco et al. [7], while the disappearance of the second local maximum is related to the weakening of the impinging vortex rings

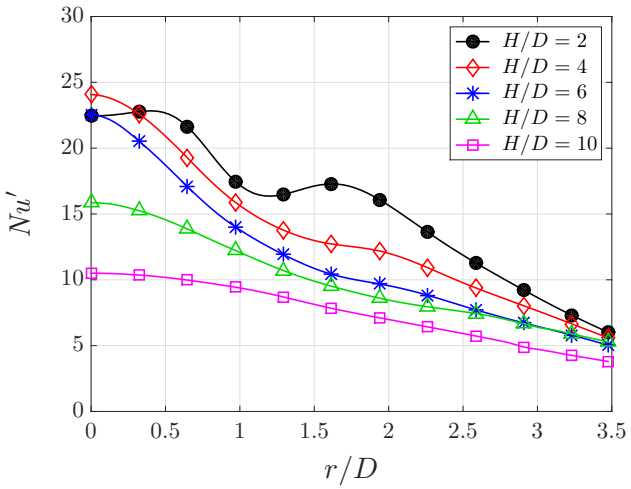

Figure 7: Radial distribution of Nusselt number standard deviation for $L_0/D = 20$ and each H/D (i.e., 2, 4, 6, 8 and 10) at Reynolds number equal to 5,250.

[23]. As a matter of fact, both the primary vortex ring and those vortex rings caused by the Kelvin-Helmholtz instability of the trailing jet impinge on the plate with lower strength and, consequently, they generate weaker secondary vortex rings. At $H/D = 6$, the Nu' profile does not significantly change, apart from the outer inflection point which almost disappears, while, at higher nozzle-to-plate distances, the Nu' values continue decreasing because the synthetic jet is approaching a steady condition [24].

At $L_0/D = 10$ (Figure 8), the values of Nu' are lower than those at $L_0/D = 20$ for $H/D \leq 6$, while they are practically similar at higher dimensionless nozzle-to-plate distances. The observed difference could be ascribed to the value of the phase correlated kinetic energy defined and discussed by Greco et al. [23]. Indeed, the higher dimensionless stroke length causes a stronger organized perturbation in the flow field which is "felt" more on the impingement plate, at a fixed nozzle-to-plate distance, causing a larger fluctuation of the Nusselt number. Analysing the Nu' behaviour, in the case $L_0/D = 10$ at $H/D = 2$, it is worth noting the local maximum located at r/D equal to 0.52. This maximum reveals the presence of the inner ring-shaped region caused by the impinging

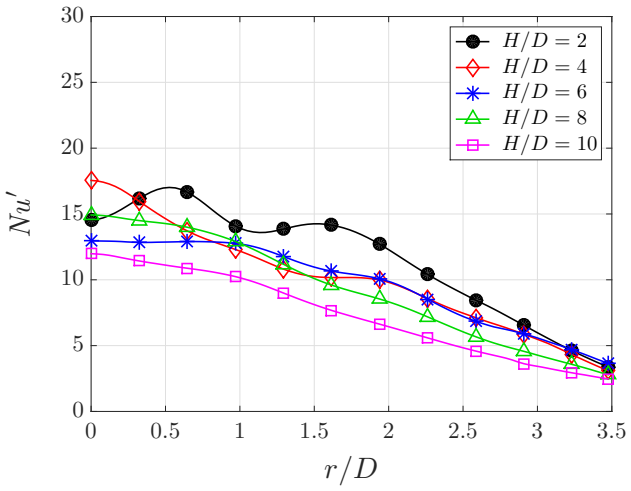

Figure 8: Radial distribution of Nusselt number standard deviation for $L_0/D = 10$ and each H/D (i.e., 2, 4, 6, 8 and 10) at Reynolds number equal to 5,250.

potential core, as for the case at $L_0/D = 20$, but, contrarily to the latter case, the outer ring-shaped region (present at $r/D = 1.5$) is not so strong. This is due to the generation process of the secondary vortex ring near the impingement plate. As a matter of fact, secondary vortex rings are principally initiated by the primary vortex ring [23, 33], whereas, differently from the case $L_0/D = 20$, vortex rings generated by the Kelvin-Helmholtz instability along the shear layer of the trailing jet are not strong enough to generate further secondary vortex rings. Indeed, at $L_0/D = 10$, the presence and the influence of the trailing jet on both the flow field and heat transfer weakens. At $H/D = 4$, the Nu' maximum is observed at the stagnation point, because of the limited extent of the potential-core region, while a local maximum is still visible at $r/D = 1.75$ before the final decrease. At $H/D = 6$, the Nu' distribution shows a plateau up to $r/D \approx 1$ before the monotonic decrease, very similar to case at $L_0/D = 5$. At higher nozzle-to-plate distances, the Nu' profile tends to attain the same distribution observed at $L_0/D = 20$.

At $L_0/D = 5$ (Figure 9), the values of Nu' are the lowest, because of the weaker organized perturbation introduced in the flow field. Furthermore, these

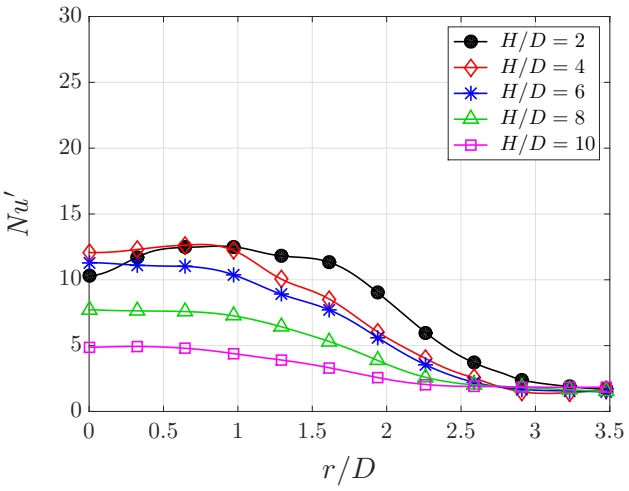

Figure 9: Radial distribution of Nusselt number standard deviation for $L_0/D = 5$ and each H/D (i.e., 2, 4, 6, 8 and 10) at Reynolds number equal to 5,250.

values decrease as the nozzle-to-plate distance increases, because the synthetic jet is turning into a steady turbulent jet [24], while the phase-correlated kinetic energy decreases. The main feature of the Nu' distribution, at the shortest nozzle-to-plate distance, is the local minimum at the stagnation point and the local maximum located at $r/D = 0.9$. The position of this peak could depend on the radial location where the impinging vortex ring core is closer to the impingement plate [23] causing a greater fluctuation of the Nusselt number. At $H/D = 4$, the Nu' distribution shows a plateau at $r/D \leq 0.9$ before decreasing. Such a plateau is still visible at $H/D = 6$, but the Nu' values are lower. At higher H/D, the Nu' values continue decreasing because the synthetic jet has turned in a quasi-steady jet, in agreement with Krishnan and Mohseni [52].

3.2. Phase-averaged results

In Figure 10, the Nu_φ distribution, at $H/D = 2$ and $L_0/D = 20$, is shown. At $\varphi = 0°$, the primary vortex ring of the synthetic jet starts affecting the Nu distribution on the impingement plate. As the phase increases ($\varphi = 36°$), the vortex ring approaches the plate, and Nu_φ increases near the stagnation

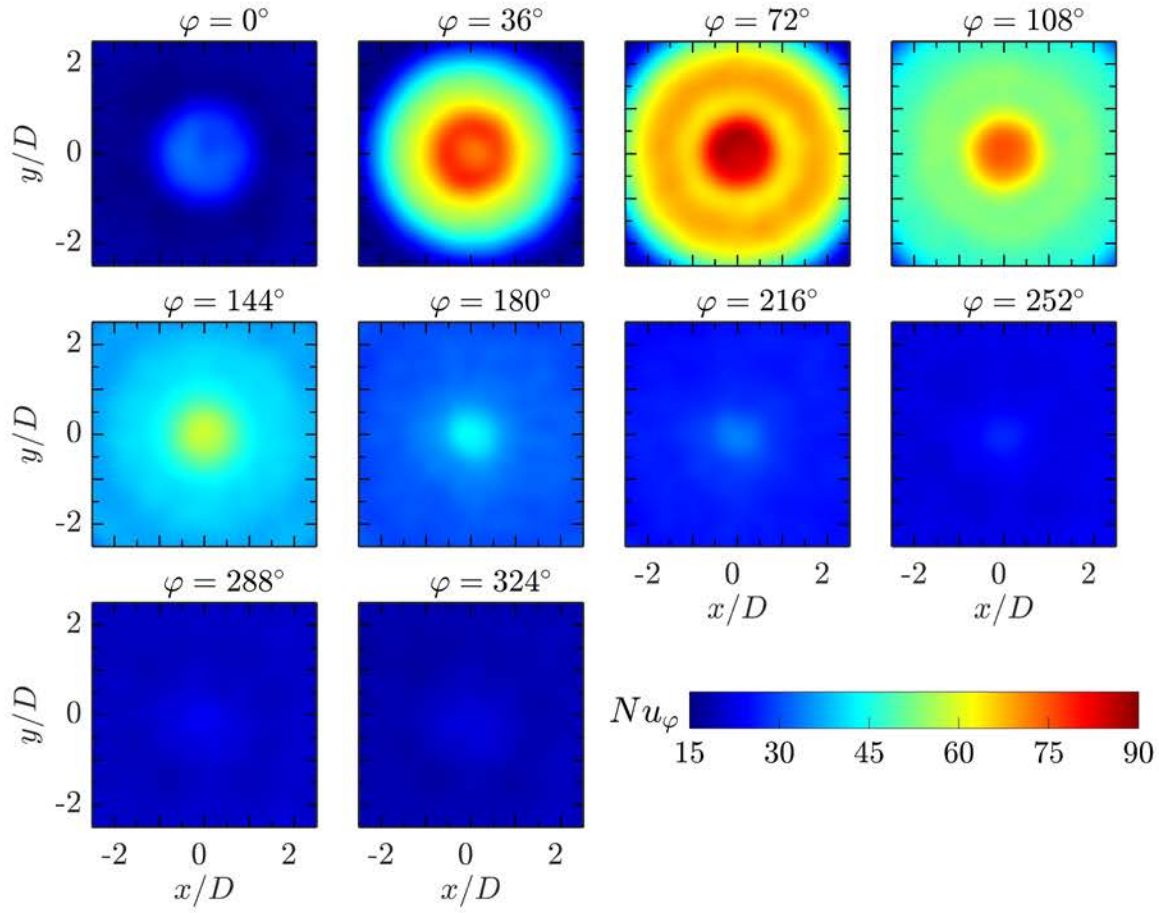

Figure 10: Phase-averaged Nusselt number at $L_0/D = 20$, $H/D = 2$ and $Re = 5,250$.

point, barely showing an inner ring-shaped region of maximum heat transfer. At $\varphi = 72°$, the phase-averaged Nusselt number continues increasing and the region characterized by high Nu_φ widens because the jet is spreading over the impingement plate. At this phase, the Nu_φ distribution is clearly characterized by an inner and an outer ring-shaped region of maximum Nusselt number located at $r/D = 0.35$ and 1.75, respectively. As aforementioned, the inner ring-shaped region is related to the radial acceleration of the wall jet inside the stagnation region, while the outer ring-shaped region is due to the presence of the secondary vortex ring initiated by the primary vortex ring. At the following phase (i.e., $\varphi = 108°$), in addition to the inner ring-shaped region, two outer ring-shaped regions are observed at $r/D = 1.7$ and $r/D = 2.75$ (this latter is partially visible in the corners of the field of view). This external outer ring-shaped region is still related to the secondary vortex ring generated by the primary vortex, whereas the internal one ($r/D = 1.7$) is ascribed to the secondary vortex rings originated by the adverse pressure gradient induced by the trailing jet Kelvin-Helmholtz vortex rings. Passing to $\varphi = 144°$, the Nu_φ values in the stagnation region decrease and the inner ring-shaped region is replaced by a bell-shaped distribution in the proximity of the jet centerline, while the farthest outer ring-shaped region is outside of the field of view. At $\varphi \geq 144°$, the values of Nu_φ over the stagnation region continue decreasing.

The evolution of the Nu_φ distribution, at $H/D = 10$ and $L_0/D = 20$, is represented in Figure 11. The phase-averaged Nusselt number increases up to $\varphi = 72°$ as well as the extent of the high heat transfer region. At $\varphi = 108°$ the Nusselt number distribution near the stagnation region does not show the inner ring-shaped region, while the primary vortex ring causes a local heat transfer maximum at $r/D = 1.8$ through the formation of a secondary vortex ring. Such a local maximum is definitely lower than that observed at $H/D = 2$ (at $\varphi = 72°$) because the primary vortex ring, and correspondingly the secondary vortex ring, are weaker. Furthermore, no outer ring-shaped region, caused by trailing jet Kelvin-Helmholtz vortices, is present because of their strong weakening. As the phase increases, Nu_φ decreases, exhibiting a bell-shaped distribution in the

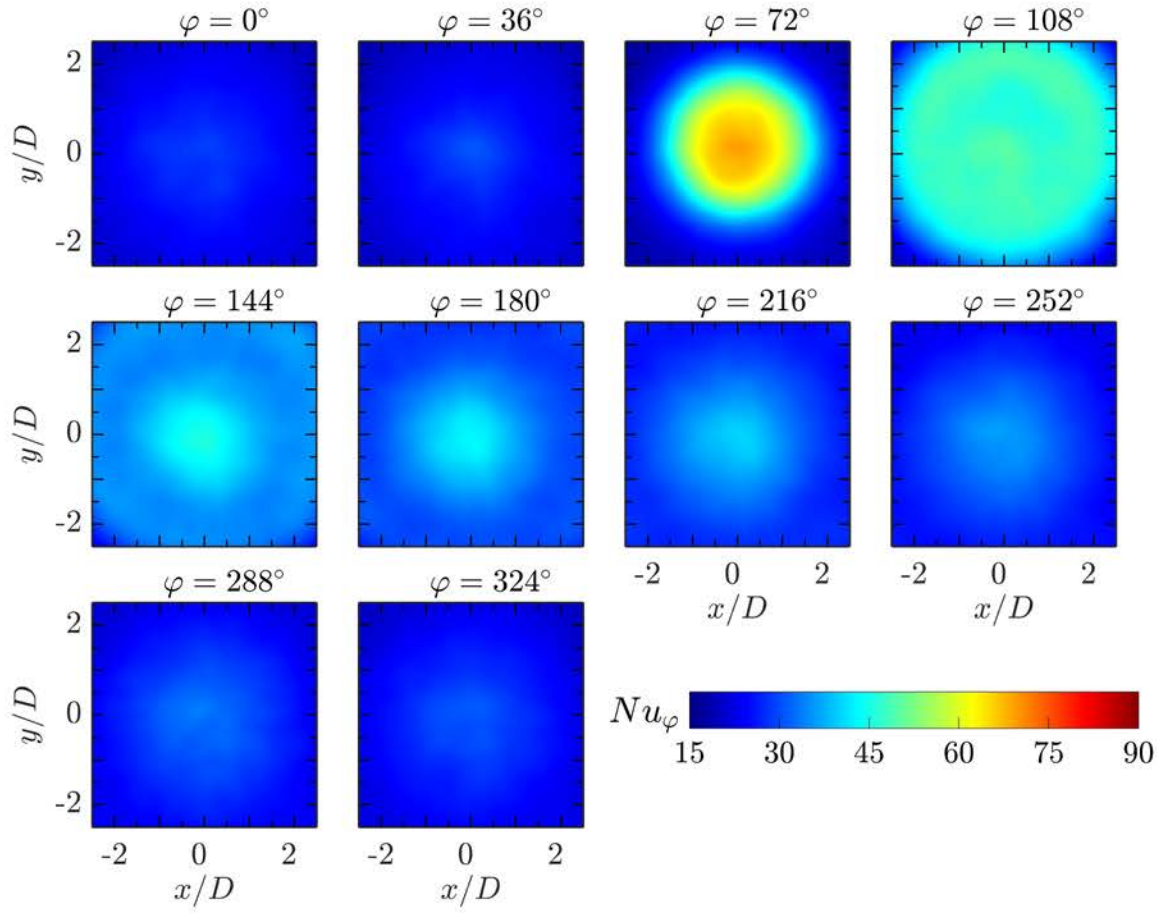

Figure 11: Phase-averaged Nusselt number at $L_0/D = 20$, $H/D = 10$ and $Re = 5,250$.

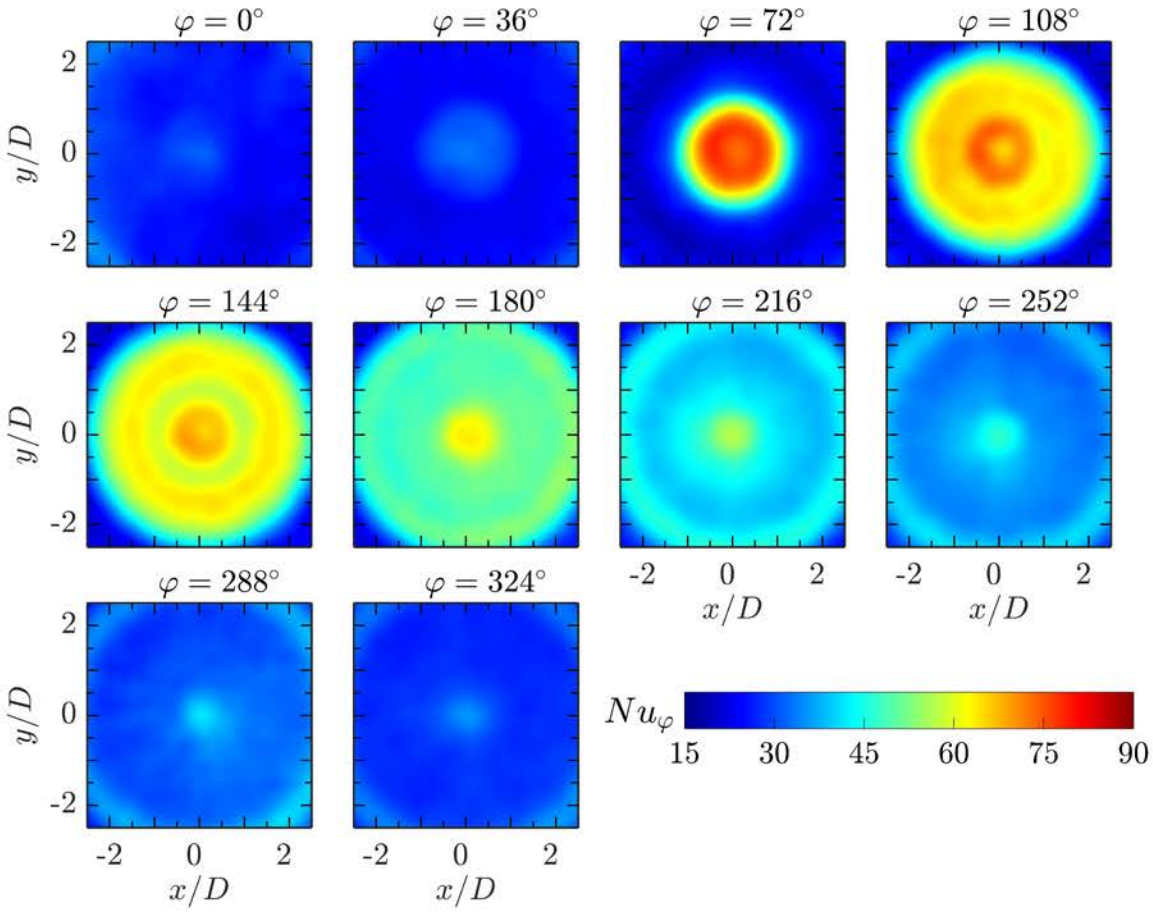

Figure 12: Phase-averaged Nusselt number at $L_0/D = 10$, $H/D = 2$ and $Re = 5,250$.

stagnation region, and the outer ring-shaped region widens, while the vortex ring sweeps across the plate. At this nozzle-to-plate distance, the outer ring-shaped region has already exited the field of view at $\varphi = 180°$.

The phase-averaged heat transfer behaviour, at $H/D = 2$ and $L_0/D = 10$, is shown in Figure 12. At $\varphi = 0°$, Nu_φ starts increasing in the stagnation point and, simultaneously, an outer ring-shaped region of local heat transfer maximum is visible, in the corners of the field of view, at $r/D = 2.85$. The latter is caused by the sweeping vortex ring generated during the previous ejection phase. In this configuration, differently from the highest stroke length case,

such an outer ring-shaped region is still visible at $\varphi = 0°$ because the spacing between two successive vortex rings decreases with decreasing stroke length [24]. From $\varphi = 36°$ to $\varphi = 72°$, the outer ring-shaped region moves outwards, while, simultaneously, the Nu_φ values increase in the stagnation region reaching their maximum. In the latter phase (i.e., $\varphi = 72°$), an inner ring-shaped region at $r/D = 0.5$ is barely visible. At φ equal to 108° and 144°, the Nu_φ values near the stagnation region decrease but the inner ring-shaped region is now clearly visible and also the outer ring-shaped region is present. Contrary to the highest stroke length configuration (see $\varphi = 108°$ Figure 10), only one outer ring-shaped region is present because the primary vortex ring is much stronger than the trailing jet and its Kelvin-Helmholtz vortex rings. Indeed, during these phases, the Nusselt number contribution of the primary vortex ring attains the same value as that ascribed to the impinging trailing jet, in contrast with what observed for $L_0/D = 20$ and $H/D = 2$. For $\varphi \geq 180°$, the values of Nu_φ, in the stagnation region, decrease and the inner ring-shaped region disappears, while the outer ring-shaped region outlives, broadening above the plate.

The evolution of the Nu_φ distribution, at $H/D = 10$ and $L_0/D = 10$, is represented in Figure 13. The phase-averaged Nusselt number increases up to $\varphi = 108°$ along with the extent of the high Nusselt number region. At $\varphi = 144°$, the Nusselt number distribution does not show any inner ring-shaped region, but the heat transfer maximum, caused by the primary vortex ring through the formation of a secondary vortex ring, is visible at $r/D = 1.7$. This local heat transfer maximum is the unique outer ring-shaped region, because those originated by trailing jet Kelvin-Helmholtz vortices are not present due to their strong weakening. As the phase increases, Nu_φ in the stagnation region decreases and the outer ring-shaped region widens, while the vortex ring sweeps across the plate.

In Figure 14, the Nu_φ distribution, at the lowest dimensionless stroke length at $H/D = 2$, is shown. Contrary to the case of the highest L_0/D (Figure 10), the Nu_φ distribution at $\varphi = 0°$ is characterized by the increasing Nusselt number value in the stagnation point and by an outer ring-shaped region of maximum

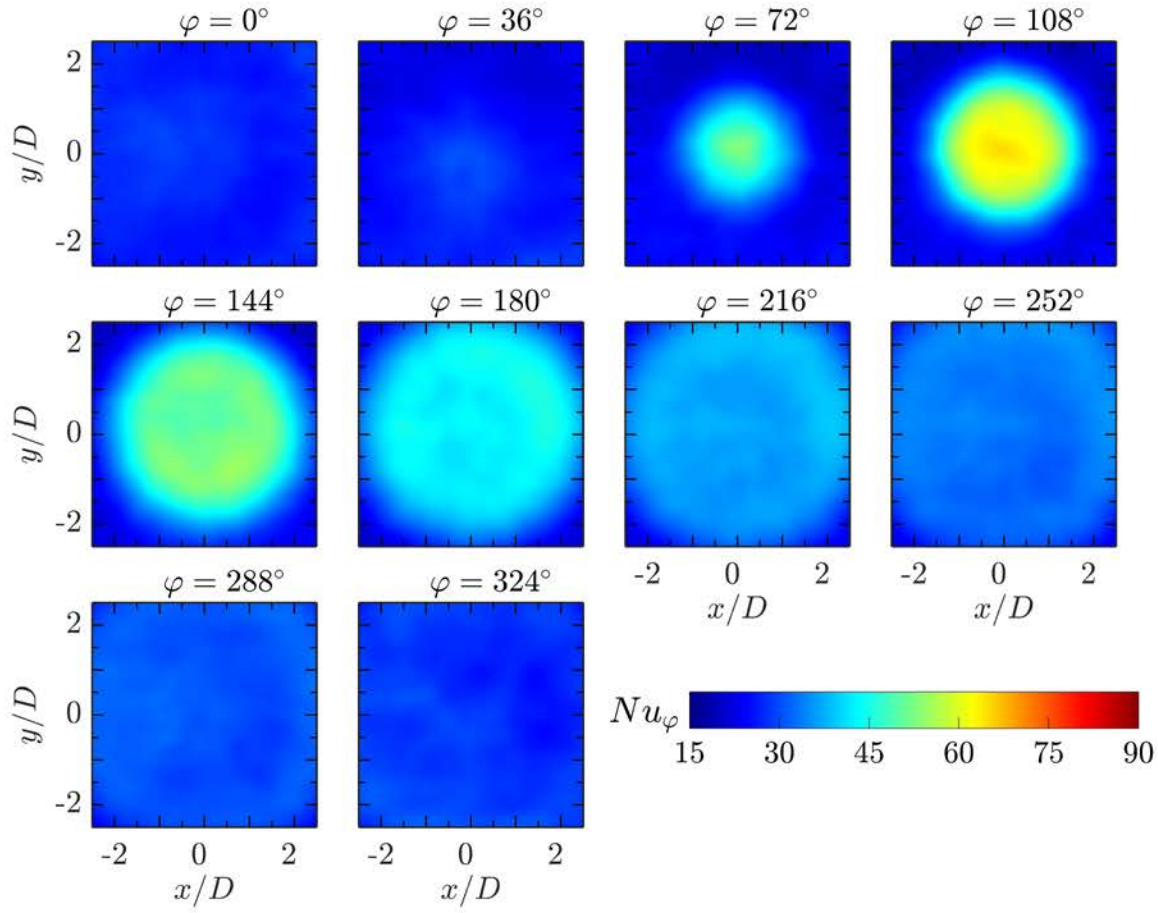

Figure 13: Phase-averaged Nusselt number at $L_0/D = 10$, $H/D = 10$ and $Re = 5,250$.

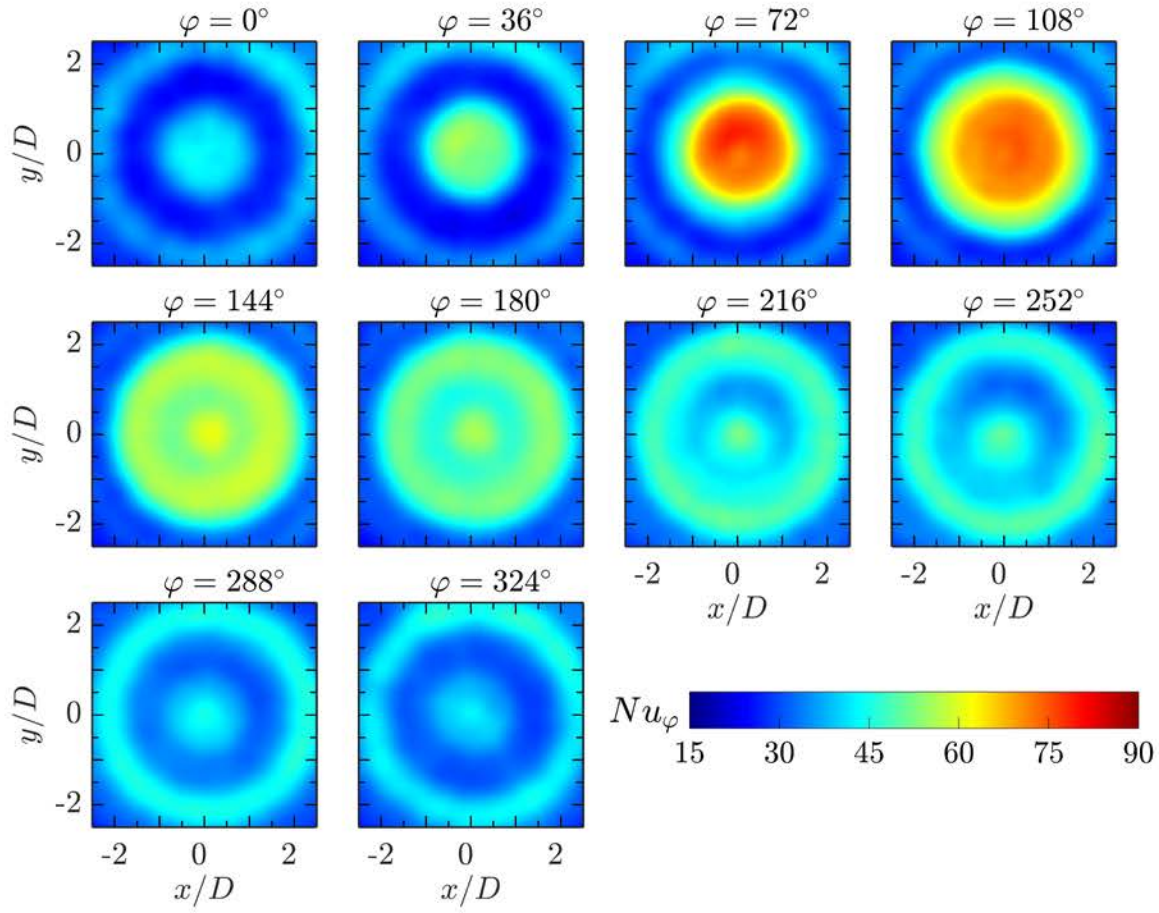

Figure 14: Phase-averaged Nusselt number at $L_0/D = 5$, $H/D = 2$ and $Re = 5,250$.

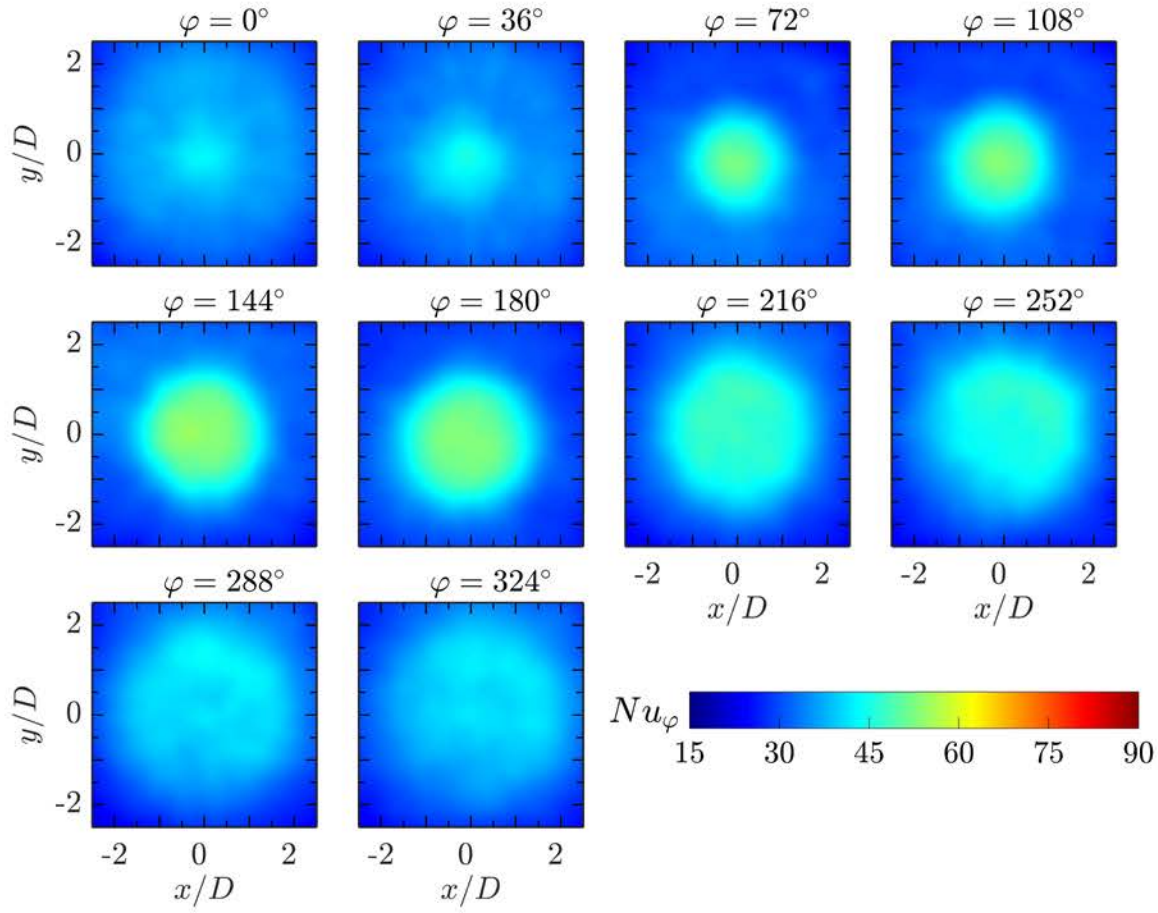

Figure 15: Phase-averaged Nusselt number at $L_0/D = 5$, $H/D = 10$ and $Re = 5,250$.

heat transfer Nusselt number $r/D = 2.2$, which is analogous to what observed for $L_0/D = 10$ (Figure 12). Such an outer ring-shaped region of maximum heat transfer is closer to the stagnation region than that observed at $L_0/D = 10$, because of the lower value of the dimensionless stroke length [24]. As the phase increases, the ring-shaped region of maximum heat transfer moves outward and weakens. Simultaneously, the region near the stagnation point, characterized by high Nu_φ values, broadens attaining greater values of Nu_φ up to $\varphi = 108°$. For $\varphi \geq 144°$, Nu_φ decreases in the stagnation region, while the ring-shaped region of maximum heat transfer moves along the radial direction. In opposition to the two highest stroke length configurations, no inner ring-shaped region of maximum heat transfer is detected. In addition to that, the unique outer ring-shaped regions of maximum heat transfer are those associated with the presence of primary vortex rings, similar to $L_0/D = 10$ case.

At higher nozzle-to-plate distance (i.e., $H/D = 10$), the Nu evolution of the synthetic jet, with $L_0/D = 5$, is characterized by different phenomena, as reported in Figure 15. At $\varphi = 0°$, a distribution of fairly high Nu_φ is already present, because the synthetic jet, characterized by $L_0/D = 5$, has already turned into a quasi-steady turbulent jet at this distance from the exit plane, in agreement with Krishnan and Mohseni [52]. Indeed, analysing the entire evolution of the Nu_φ distribution, it is possible to point out that a slight heat transfer fluctuation is still present, but it is much lower than those observed at lower H/D and/or higher L_0/D. In particular, it is worth noting that no outer ring-shaped regions of maximum heat transfer are observed because of the strong weakening of the primary vortex ring.

4. Conclusions

The steady and unsteady heat transfer behaviour of an impinging synthetic jet has been analysed for three different values of the dimensionless stroke length by means of the IR Thermography technique and a heated thin foil sensor. Through a careful comparison with previous works about the impinging flow

field of synthetic jets, the present investigation highlights how the topology of the impinging synthetic jet flow field, which depends essentially on L_0/D, influences the heat transfer mechanisms at the impingement plate, resulting in different performances when the distance between the plate and the nozzle exit section is varied. At the highest L_0/D (i.e., $L_0/D = 20$), the heat transfer behaviour resembles that of a continuous jet. The time-averaged stagnation Nusselt number is found to increase with the nozzle-to-plate distance, achieving a maximum at $4 < H/D < 6$, and both inner and outer ring-shaped regions of maximum heat transfer are observed in the mean Nusselt distribution at small H/D. As the distance from the impingement plate increases, the Nu radial profile approaches a bell-shaped distribution. The disappearance of the inner ring-shaped region is due to the limited extent of the potential-core-like region, which causes the jet to come to impingement, from a certain distance onward, with a non-uniform (Gaussian-shaped) velocity profile. Instead, the disappearance of the outer ring-shaped regions is caused by the weakening of the secondary vortex rings initiated by the impinging vortex rings (both the primary and the trailing-jet Kelvin-Helmholtz ones). Moreover, the phase-correlated Nusselt number fluctuations decrease with H/D since, while moving downstream, the synthetic jet turns into a steady turbulent flow characterized by a low level of phase organization.

For shorter L_0/D, the time-averaged stagnation Nusselt number maximum is reached at lower H/D consistently with the shortening or disappearance of the potential-core-like region. Similarly, the inner ring-shaped region of maximum heat transfer is visible but weaker ($L_0/D = 10$) or totally absent ($L_0/D = 5$) also at small H/D. For both these configurations, outer ring-shaped regions of maximum heat transfer are mainly generated by secondary vortex rings originated by the primary vortices of the synthetic jet. Indeed, since the extent of the trailing jet decreases with decreasing stroke length, at short L_0/D the heat transfer process is not influenced by Kelvin-Helmholtz vortex rings inherent to the trailing jet itself, which are weaker ($L_0/D = 10$) or totally absent ($L_0/D = 5$). In addition, the decrease of L_0/D causes a weaker organized wave

in the flow field resulting in a less unsteady turbulent jet and, subsequently, in a drop of the Nusselt number fluctuations. The phase-averaged measurements show that the periodic evolution of the heat transfer is, in fact, dominated by the impingement and interaction of the synthetic jet vortex rings and their trailing jets with the impingement plate. Also in the phase-averaged Nusselt number maps, it is possible to detect ring-shaped regions of maximum heat transfer at small H/D, replaced by a bell-shaped distribution at high H/D. In particular, the presence of a prominent trailing jet at high L_0/D causes, at small H/D, the formation of an inner and outer-shaped ring regions of maximum heat transfer, similarly to what happens in the unsteady evolution of continuous jets. In addition to these regions, the impingement of the synthetic jet vortex ring results in a further outer ring-shaped region, which is more external and has a greater longevity in the phase evolution since the primary vortex ring is stronger than the trailing-jet Kelvin-Helmholtz ones. At low L_0/D, owing to the reduction or disappearance of the trailing jet, the phase evolution is completely dominated by the impingement of the synthetic jet vortex rings. Outer ring-shaped regions are observed in the Nu_φ distribution, simultaneously to the beginning of the impingement phase, because of the reduced spacing between the vortex rings. However, at high H/D, such regions disappear after the weakening of the primary vortex rings, and the distribution of the Nusselt number tends to a steady bell-shaped profile.

Acknowledgements

The authors wish to thank Mr. G. Sicardi for contributing the realization of the experimental setup. Carlo Salvatore Greco, Andrea Ianiro and Gennaro Cardone have been partially supported by Grant DPI2016-79401-R funded by the Spanish State Research Agency (SRA)and European Regional Development Fund (ERDF).

References

1. Martin, H.. Heat and mass transfer between impinging gas jets and solid surfaces. *Adv Heat Tran* 1977;13:1–60.

2. Jambunathan, K., Lai, E., Mossand, M.A., Button, B.L.. A review of heat transfer data for single circular jet impingement. *Int J Heat Fluid Fl* 1992;13:106–115.

3. Carlomagno, G.M., Ianiro, A.. Thermo-fluid-dynamics of submerged jets impinging at short nozzle-to-plate distance: A review. *Exp Therm Fluid Sci* 2014;58:15–35.

4. Chaudhari, M., Puranik, B., Agrawal, A.. Heat transfer characteristics of synthetic jet impingement cooling. *Int J Heat Mass Tran* 2010;53:1057–1069.

5. Valiorgue, P., Persoons, T., McGuinn, A., Murray, D.B.. Heat transfer mechanisms in an impinging synthetic jet for small jet-to-surface spacing. *Exp Therm Fluid Sci* 2009;33:597–603.

6. Bhapkar, U.S., Srivastava, A., Agrawal, A.. Acoustic and heat transfer aspects of an inclined impinging synthetic jet. *Int J Therm Sci* 2013;74:145–155.

7. Greco, C.S., Ianiro, A., Cardone, G.. Time and phase average heat transfer in single and twin circular synthetic impinging air jets. *Int J Heat Mass Tran* 2014;73:776–788.

8. Gallas, Q., Holman, R., Nishida, T., Carroll, B., Sheplak, M., Cattafesta, L.. Lumped element modeling of piezoelectric-driven synthetic jet actuators. *AIAA J* 2003;41(2):240–247.

9. Persoons, T.. General reduced-order model to design and operate synthetic jet actuators,. *AIAA J* 2012;50(4):916–927.

10. de Luca, L., Girfoglio, M., Coppola, G.. Modeling and experimental validation of the frequency response of synthetic jet actuators. *AIAA J* 2014;52(8):1733–1748.

11. de Luca, L., Girfoglio, M., Chiatto, M., Coppola, G.. Scaling properties of resonant cavities driven by piezo-electric actuators. *Sensor Actuat A-Phys* 2016;247:465–474.

12. Holman, R., Utturkar, Y., Mittal, R., Smith, B.L., Cattafesta, L.. Formation criterion for synthetic jets. *AIAA J* 2005;43(10):2110–2116.

13. Smith, B.L., Glezer, A.. The formation and evolution of synthetic jets. *Phys Fluids* 1998;10(9):2281–2297.

14. Cater, J.E., Soria, J.. The evolution of round zero-net-mass-flux jets. *J Fluid Mech* 2002;472:167–200.

15. Gutmark, E., Yassour, Y., Wolfshtein, M.. Acoustic enhancement of heat transfer in plane channels. *Proceedings of Seventh International Heat Transfer Conference, Munich, Germany* 1982;:441–445.

16. Mahalingam, R., Glezer, A.. Design and thermal characteristics of a synthetic jet ejector heat sink. *J Electron Packaging* 2005;127:172–177.

17. Bazdidi-Therani, F., Karami, M., Jahromi, M.. Unsteady flow and heat transfer analysis of an impinging synthetic jet. *Heat Mass Trans* 2011;47:1363–1373.

18. Silva-Lanca, L., Ortega, A., Rose, I.. Experimental convective heat transfer in a geometrically large two-dimensional impinging synthetic jet. *Int J Therm Sci* 2015;90:339–350.

19. Zhang, J., Tan, X.. Experimental study on flow and heat transfer characteristics of synthetic jet driven by piezoelectric actuator. *Sci China Ser E* 2007;50(2):221–229.

20. Arik, M., Icoz, T.. Predicting heat transfer from unsteady synthetic jets. *J Heat Transfer* 2012;134:1–8.

21. Persoons, T., McGuinn, A., Murray, D.B.. A general correlation for the stagnation point Nusselt number of an axisymmetric impinging synthetic jet. *Int J Heat Mass Tran* 2011;54:3900–3908.

22. McGuinn, A., Farrelly, R., Persoons, T., Murray, D.B.. Flow regime characterisation of an impinging axisymmetric synthetic jet. *Exp Therm Fluid Sci* 2013;47:241–251.

23. Greco, C.S., Cardone, G., Soria, J.. On the behaviour of impinging zero-net-mass-flux jets. *J Fluid Mech* 2017;810:25–59.

24. Shuster, J.M., Smith, D.R.. Experimental study of the formation and scaling of a round synthetic jet. *Phys Fluids* 2007;19(4):045109.

25. Silva-Lanca, L., Ortega, A.. Vortex dynamics and mechanisms of heat transfer enhancement in synthetic jet impingement. *Int J Therm Sci* 2017;112:153–164.

26. Trávníček, Z., Vít, T.. Impingement heat/mass transfer to hybrid synthetic jets and other reversible pulsating jets. *Int J Heat Mass Tran* 2015;85:473–487.

27. Garg, J., Arik, M., Weaver, S., Wetzel, T.. Meso scale pulsating jets for electronics cooling. *J Electron Packag* 2005;127(4):503–511.

28. Gillespie, M.B., Black, W.Z., Rinehart, C., Glezer, A.. Local convective heat transfer from a constant heat flux flat plate cooled by synthetic air jets. *J Heat Transfer* 2006;128(10):990–1000.

29. Amitay, A.P.M.. Electronic cooling using synthetic jet impingement. *J Heat Transfer* 2006;128(9):897–907.

30. Arik, M.. An investigation into feasibility of impingement heat transfer and acoustic abatement of meso scale synthetic jets. *Appl Therm Eng* 2007;27(8):1483–1494.

31. Ghaffari, O., Ikhlaq, M., Arik, M.. An experimental study of impinging synthetic jets for heat transfer augmentation. *Int J Air-Cond Refrig* 2015;23(3):1550024.

32. Ghaffari, O., Solovitz, S.A., Arik, M.. An investigation into flow and heat transfer for a slot impinging synthetic jet. *Int J Heat Mass Tran* 2016;100:634–645.

33. Greco, C.S., Castrillo, G., Crispo, M.C., Astarita, T., Cardone, G.. Investigation of impinging single and twin circular synthetic jets flow field. *Exp Therm Fluid Sci* 2016;74:354–367.

34. Carlomagno, G.M., Cardone, G.. Infrared thermography for convective heat transfer measurements. *Exp Fluids* 2010;49:1187–1218.

35. Nakamura, H.. Frequency response and spatial resolution of a thin foil for heat transfer measurements using infrared thermography. *Int J Heat Mass Tran* 2009;52(21):5040–5045.

36. Greco, C.S., Ianiro, A., Astarita, T., Cardone, G.. On the near field of single and twin circular synthetic air jets. *Int J Heat Fluid Fl* 2013;44:41–52.

37. Raiola, M., Greco, C.S., Contino, M., Discetti, S., Ianiro, A.. Towards enabling time-resolved measurements of turbulent convective heat transfer maps with IR thermography and a heated thin foil. *Int J Heat Mass Tran* 2017;108:199–209.

38. Carlomagno, G.M., de Luca, L.. Infrared thermography in heat transfer. *Handbook of flow visualization* 1989;:531–553.

39. Meola, C., de Luca, L., Carlomagno, G.M.. Azimuthal instability in an impinging jet: adiabatic wall temperature distribution. *Exp Fluids* 1995;18(5):303–310.

40. Meola, C., de Luca, L., Carlomagno, G.M.. Influence of shear layer dynamics on impingement heat transfer. *Exp Therm Fluid Sci* 1996;13(1):29–39.

41. Violato, D., Ianiro, A., Cardone, G., Scarano, F.. Three-dimensional vortex dynamics and convective heat transfer in circular and chevron impinging jets. *Int J Heat Fluid Fl* 2012;37:22–36.

42. Ianiro, A., Cardone, G.. Heat transfer rate and uniformity in multichannel swirling impinging jets. *Appl Therm Eng* 2012;49:89–98.

43. Cafiero, G., Castrillo, G., Greco, C.S., Astarita, T.. Effect of the grid geometry on the convective heat transfer of impinging jets. *Int J Heat Mass Tran* 2017;104:39–50.

44. Astarita, T., Carlomagno, G.M.. Infrared Thermography for Thermo-Fluid-Dynamics. Springer; 2012.

45. Carlomagno, G.M., Discetti, S., Astarita, T.. Experimental assessment of a new heat flux sensor for measuring convective heat transfer coefficients. *QIRT J* 2011;8(1):37–49.

46. McAdams, W.. Heat Transmission. New York, NY: 3rd Ed. McGraw-Hill; 1954.

47. Welty, J., Wicks, C., Rorrer, G., Wilson, R.. Fundamentals of momentum, heat and mass transfer. John Wiley and Sons; 2009.

48. Moffat, R.. Describing the uncertainties in experimental results. *Exp Therm Fluid Sci* 1988;1:3–17.

49. Abramovich, G.. The Theory of Turbulent Jets. M.I.T. Press; 1963.

50. Mallinson, S.G., Hong, G., Rezeis, J.A.. Some characteristics of synthetic jets. *AIAA paper* 1999;:3651.

51. Rohlfs, W., Haustein, H.D., Garbrecht, O., Kneer, R.. Insights into the local heat transfer of a submerged impinging jet: Influence of local flow acceleration and vortex-wall interaction. *Int J Heat Mass Tran* 2012;55:7728–7736.

52. Krishnan, G., Mohseni, K.. Axisymmetric synthetic jets: An experimental and theoretical examination. *AIAA J* 2009;47(10):2273–2283.